Supporting Information of

Activating the Oxide Pathway Mechanism via Selective Intralayer Cl Coordination with Ni/Fe Sites of Hydroxides for Robust Water Oxidation

Guanwen Wang[1, 2], Chunlei Chi[2], Yufei Zhou[1, 2], Baoyi Mu[1, 2], Qiushi Miao[1, 2], Bin Qi[1, 2], Xinhou Yang[1], Fan Feng[2], Liang Wu[1], Xinxin Zhao[1], Yichao Huang*[2], Chuanqing Wang*[1], Tong Wei*[1, 2], and Zhuangjun Fan*[1, 2]

[1]Institute of Energy, Hefei Comprehensive National Science Center, Hefei 230051, China
[2]Shandong Key Laboratory of Intelligent Energy Materials, School of Material Science and Engineering, China University of Petroleum (East China), Qingdao 266580, China

Catalysts preparation

$NiFe(OH)_xCl_y$@NF was prepared via solvent thermal treatment. Specifically, 0.79 g (3.33 mmol) $NiCl_2·6H_2O$ and 1.08 g (6.67 mmol) $FeCl_3$ were added with a molar ratio of 1:2 to the solution, which consisted of 80 mL of ethanol and 20 mL of deionized water. The solution was transferred to a Teflon-lined autoclave and heated for 36 hours at 200 °C with a pre-treated 5×5 cm^2 NF substrate. The product was washed by deionized water and dried at 80 °C, exhibiting an average loading of 5.8 mg cm^{-2}. The $NiFeO_xH_y$@NF catalyst was synthesized via a conventional hydrothermal coprecipitation method. Specifically, 0.87 g of $Ni(NO_3)_2·6H_2O$, 2.42 g of $Fe(NO_3)_3·9H_2O$, and 1.68 g of urea were dissolved in 15 mL of deionized water under stirring to form a homogeneous precursor solution. The resulting solution was then transferred into a Teflon-lined autoclave, together with a pretreated 5×5 cm^2 nickel foam substrate. The hydrothermal reaction was carried out at 150 °C for 24 h. After naturally cooling to room temperature, the sample was collected, thoroughly rinsed with deionized water, and then dried at 80 °C to obtain the $NiFeO_xH_y$@NF. The average loading of $NiFeO_xH_y$ on NF was determined to be 2.3 mg cm^{-2}. Both of these catalyst powder (denoted as "$NiFe(OH)_xCl_y$" and "$NiFeO_xH_y$") was synthesized in the corresponding method without the addition of NF. RuO_2@NF was prepared via a dip-coating approach. Firstly, 5.0 mg of commercial RuO_2 powder was dispersed in a mixture of 475 μL deionized water, 475 μL isopropanol, and 50 μL Nafion solution, followed by ultrasonication for 30 minutes. The suspension was then drop-cast onto the NF substrate and dried under an infrared lamp. Finally, the electrode was vacuum-dried at 80 °C for 12 hours to obtain the RuO_2@NF catalyst.

Characterizations

The morphology and structure of the samples were characterized by the scanning electron microscope (SEM, ZEISS, Sigma 360) with an acceleration voltage of 15 kV. Aberration-corrected scanning transmission electron microscopy (Ac-STEM, Thermo Fisher, Titan Themis G2 300) with an acceleration voltage of 300 kV. X-ray photoelectron spectroscopy (XPS) measurements were carried out with a Thermo

Fisher Scientific Escalab 250Xi System with monochromatic Al Kα radiation (energy 1486.6 eV) calibrated by referencing the C 1s to 284.8 eV. UV-vis spectra were recorded on a spectrometer (UV-2700, Shimadzu, Japan). EPR spectra were obtained by Bruker EMXplus-6/1. Ultraviolet photo-electron spectroscopy (UPS) was conducted with a Thermo Fisher Escalab Xi+ System with He I radiation ($h\nu$=21.22 eV) under the bias voltage of -5 V. The energy vs. vacuum energy level ($E_{vs.\ Vac}$) should be calibrated by the energy vs. RHE ($E_{vs.\ RHE}$) by the following equation:

$$E_{vs.\ Vac} = E_{vs.\ RHE} + (-4.44 - 0.059 \times pH) \quad (1)$$

Where -4.44 represents the energy gap from RHE (pH=0) to the vacuum energy level[1]. When pH=14, the gap was calculated to be -5.27 eV. The relationship between E_{CBM}, E_{VBM} and E_g was summarized:

$$E_{VBM} = E_{CBM} - E_g \quad (2)$$

Where E_{CBM} could be detected from the value of flat band potential (E_{fb}) in Mott-Schottky plots. E_g could be calculated from the Tauc analysis of Uv-vis. The E_{fermi} could be calculated by the difference value of E_{VBM} (vs. E_{fermi}) from UPS and the calculated E_{VBM} (vs. vacuum level). FTIR spectroscopy of the samples was performed on a spectrometer (Shimadzu IRTracer-100). The specific surface area and pore structure were measured by N_2 adsorption-desorption isotherm at 77.4 K (Quantachrome IQ2). The surface area was calculated by the Brunauer–Emmett–Teller (BET) method, and the pore size distribution was derived from the adsorption branches of the isotherm using the non-local density functional theory (NLDFT, a carbon model containing slit/cylindrical pore) model in the Quantachrome ASiQwin software. Inductively coupled plasma-mass spectrometry (ICP-MS) was conducted by Agilent-7900.

Chemicals

Nickel chloride hexahydrate ($NiCl_2 \cdot 6H_2O$, AR), iron chloride ($FeCl_3$, AR) and ruthenium dioxide (RuO_2, AR), sodium chloride (NaCl, AR) and ethyl alcohol were purchased from Aladdin Industrial Co., Ltd. Potassium hydroxide (KOH, AR) was supported by Beijing Chemical Corp. Pt/C catalyst was sourced from Johnson Matthey Chemicals Co., Ltd. Deionized water (18.2 MΩ·cm) was purified through Arium Pro

of Sartorius Corp. $H_2{}^{18}O$ (^{18}O abundance: 98%) was purchased from Zhengzhou Alfa Chemical Co., Ltd. Nickel foam (0.15 mm thick) was purchased from Canrd Technology Co. Ltd. To completely remove the oil and oxide layer, the nickel foam was ultrasonically pre-treated in 0.1 M HCl, deionized water, and ethanol for 15 minutes, respectively.

XAS Measurements

X-ray absorption spectroscopy data were collected at the BL14W1 station in Shanghai Synchrotron Radiation Facility (SSRF). The storage ring was working at the energy of 8.0 GeV with an average electron current of 99.5 mA. The raw data were processed using the Demeter software package. The spectra were energy-calibrated and normalized. The energy of the strongest peak of the first-order derivative of X-ray absorption near edge structure (XANES) is set to E0. The extended X-ray absorption fine structure (EXAFS) was extracted in k-space and Fourier transformed using the k3-weighted EXAFS function to amplify oscillations at high k-values. The detailed fitting parameters are shown in Tables S3 and S4. The calculation of EXAFS wavelet analysis was conducted by the FORTRAN program HAMA. The Morlet wavelet was chosen as the mother wavelet for the basic functions, and the parameters were chosen as σ=1, κ=10. All EXAFS spectra are presented without phase correction. The *operando* XAS measurements were conducted in a three-electrode configuration by applying a constant current density of 20 mA cm^{-2} to the catalyst, and XAS spectra were collected at different time

XAFS Analysis and Results

The obtained XAFS data were processed in Athena (version 0.9.26) for background, pre-edge line and post-edge line calibrations. Then, the Fourier transformed fitting was carried out in Artemis (version 0.9.26). The k^3-weighting, k-range of 3–12.5 $Å^{-1}$ and R range of 1–3 Å were used for the fitting of Ni-foil, Fe-foil, $NiFe(OH)_xCl_y$ and $NiFeO_xH_y$.

Operando Raman characterization

The Raman spectrometer (Horiba, Labram HR evolution) was utilized to test the *operando* Raman spectra. The wavelength of the excitation laser was 532 nm from a He–Ne laser. A Si wafer was used for the calibration of Raman frequencies. In the test cell, $NiFe(OH)_xCl_y$@NF acted as the working electrode, a Pt sheet was used as the counter, and the reversible hydrogen electrode (RHE) reference in 1 M KOH. Potential-dependent tests were run from OCP to 1.8 V vs. RHE on the CHI660E system.

Operando ATR-FTIR characterization

The *operando* attenuated total reflectance Fourier transform infrared spectroscopy (ATR-FTIR, PerkinElmer Spectrum. 3) was carried out by using a three-electrode setup in 1 M KOH. A total of 5 mg of $NiFe(OH)_xCl_y$ powder was transferred into a centrifuge tube, followed by the addition of 500 μL ethanol. The mixture was sealed and subjected to ultrasonication for 1 hour to ensure thorough dispersion. Subsequently, 90 μL of the suspension was drop-cast onto a silicon crystal substrate and allowed to dry under ambient conditions. The electrochemical cell was assembled using a Pt sheet as the counter electrode and the RHE electrode as the reference. KOH solution was then added as the electrolyte. The spectra were continuously collected until no significant spectral changes were observed, indicating stabilization. Then, *operando* ATR-FTIR spectra were recorded over the potential range from OCP to 1.7 V (vs. RHE).

Operando DEMS characterization

Isotope-labeled DEMS measurements were performed on a QAS 100 device (Linglu Instruments, Shanghai). RHE and Pt wire were used as the reference electrode and counter electrode, respectively. The prepared catalyst slurry was drop-cast onto a gold-coated film using a pipette. The electrolyte consisted of 1 M KOH prepared with isotopically labeled $H_2{}^{18}O$ (^{18}O-labeled water). Before measurements, the system was allowed to equilibrate for 1 minute to ensure signal stability. For the O_2 isotope labeling experiment, linear sweep voltammetry (LSV) was conducted in the potential range of 1.0–1.6 V (vs. RHE) at a scan rate of 5 mV s^{-1}. The test was repeated for 5 cycles, with

a 120-second rest period between each cycle. For the detection of Cl_2, LSV was performed under identical conditions with 60 continuous LSV cycles.

Electrochemical characterizations

Alkaline oxidation was conducted at ambient temperature using a CHI660E electrochemical workstation, and electrode stability under constant potential was evaluated with a Solartron 1470E chronoamperometry. A standard three-electrode cell was employed with $NiFe(OH)_xCl_y$@NF, $NiFeO_xH_y$@NF and RuO_2@NF as working electrodes, a reversible hydrogen electrode (RHE) as reference and a Pt sheet as counter electrode, where the potential does not need additional correction. The electrolytes—1 M KOH (pH = 14 ± 0.10) and artificial seawater (1 M KOH + 0.5 M NaCl, pH = 13.9 ± 0.15) were freshly prepared and used within 24 h, respectively. Electrochemical impedance spectroscopy was performed over 10 kHz to 0.01 Hz with an amplitude of 5 mV at open-circuit voltage. Ohmic drop was compensated using the formula:

$$E_{corr} = E - i \times R_s \times 95\% \quad (3)$$

where E is the raw potential, i is the current, and R_s is the solution resistance obtained from the intersection point of the EIS plot with the x-axis. Mott-Schottky curves were recorded in the mentioned standard three-electrode cell in 1 M KOH.

ECSA, ECSA-normalized j and mass-normalized j

The specific activity (j_{ECSA}, mA cm^{-2}) is determined by relating it to the ECSA through the equation:

$$ECSA = A \times C_{dl} / C_s \quad (4)$$

$$j_{ECSA} = j / ECSA \quad (5)$$

Where A is the geometric area of the catalyst, C_{dl} is the electrochemical double-layer capacitance measured via cyclic voltammograms in the non-Faradic range from 0.088 V to 0.098 V vs. RHE, and C_s is the specific capacitance (C_s = 0.06 mF cm^{-2}). By plotting $\Delta j/2$ at 0.093 V vs. RHE against scan rates, we estimate C_{dl} with the linear fitting slope. The mass of the loaded catalyst (m) can be determined by weighing its mass before and after the NF reaction. The mass-normalized j could be calculated

according to the following equation:

$$j_{mass} = j / m \quad (6)$$

Faradaic efficiency measurements

The Faradaic efficiency (FE) for the oxygen evolution reaction (OER) was quantified via a water-displacement gas collection system. Constant-current electrolysis was performed at 100 mA using a three-electrode configuration in 1 M KOH electrolyte. $NiFe(OH)_xCl_y$@NF and $NiFeO_xH_y$@NF were applied as the working electrode, RHE as reference and a Pt sheet as counter electrode. Evolved oxygen was collected in an inverted burette pre-filled with electrolyte, and gas volumes were measured at discrete time intervals (5, 10, 15, 20, 25, and 30 min). The theoretical oxygen yield was calculated from the total charge transfer based on Faraday's law:

$$n_{O2}(theoretical) = Q / (4 \times F) = I \times t \quad (7)$$

where F represents the Faraday constant (96485 C mol^{-1}). The FE was determined by the equation:

$$FE = n_{O2}(experimental) / n_{O2}(theoretical) \times 100\% \quad (8)$$

Triplicate measurements were conducted to ensure statistical reliability, with averaged values reported.

Theoretical calculation details

All DFT calculations were performed using the CASTEP module in Materials Studio. The Perdew-Burke-Ernzerhof (PBE) functional within the generalized gradient approximation (GGA) was employed for exchange-correlation interactions. The Brillouin zone was sampled by the Monkhorst-Pack grid as Γ-point for all systems with 2 × 2 × 1 k-points. The geometry optimization convergence criteria are set up as follows: 2.0×10^{-6} eV for energy, 0.05 eV $Å^{-1}$ for force, 550 eV for cut-off energy, and 0.002 Å for displacement. Projected density of states (PDOS) were calculated on optimized structures, with orbital-projected contributions (Ni-3d, Fe-3d, O-2p, Cl-3p) extracted for bonding analysis. The d-band centers (ε_d) were determined as the first moment of the Ni/Fe-3d PDOS:

$$\varepsilon_d = \frac{\int_{-\infty}^{+\infty} E \cdot \rho_d(E)\, dE}{\int_{-\infty}^{+\infty} \rho_d(E)\, dE} \quad (9)$$

where (E) denotes the d-orbital-resolved DOS. Crystal orbital Hamilton population (COHP) was calculated to quantify bonding/antibonding interactions between Ni/Fe and adsorbed hydroxyate atoms using the $Dmol^3$ program. Double numerical plus polarization (DNP) basis set was used with a real-space cutoff of 4.5 Å. Integrated COHP (ICOHP) provided bond-strength metrics, with negative/positive values indicating bonding/antibonding character. Adsorption energy (E) was calculated as:

$$E = E_{total} - E_{substrate} - E_{adsorbate} \quad (10)$$

Gibbs free energy (ΔG) was computed as:

$$\Delta G = \Delta E + \Delta ZPE - T\Delta S \quad (11)$$

Where ΔE is the DFT-calculated energy, ΔZPE is the zero-point energy correction, and TΔS accounts for entropy.

Assembly of AEMWE

$NiFe(OH)_xCl_y$@NF and Pt/C@NF were employed as the anode and cathode, 2 × 2 cm^2, respectively. Pt/C@NF was fabricated by a simple drop-casting method with a mass loading of 1.5 mg cm^{-2}. The anode and cathode for the electrolytic cell assembly were first positioned on their respective flow-field plates, separated using an ion exchange membrane (Versegen Tech.), and then an equal compression torque was applied. The peristaltic pump supplies 1 M KOH to both the anode and cathode at the rate of 60 mL min^{-1}. The LSV and EIS of the AEMWE were conducted on Solartron 1470E. The water electrolysis stability data of the device were recorded on a DC power supply (ITECH-6720).

Figure S1. Digital photo of 5×5 cm^2 $NiFeO_xH_y$@NF.

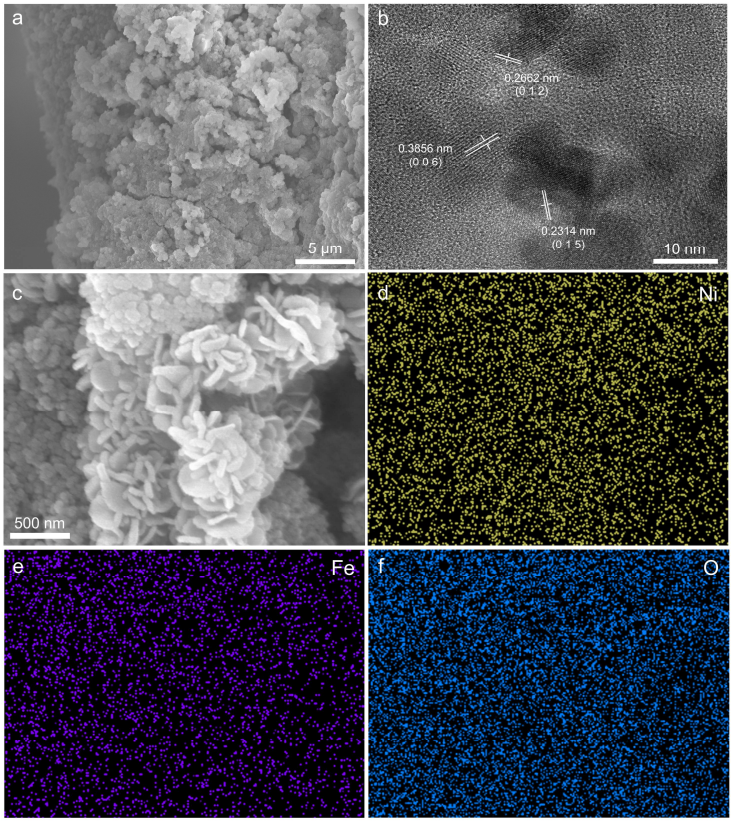

Figure S2. a) SEM image and HRTEM image of b) $NiFeO_xH_y$@NF. c) SEM image and EDS mapping images of d) Ni, e) Fe and f) O elements for $NiFeO_xH_y$@NF.

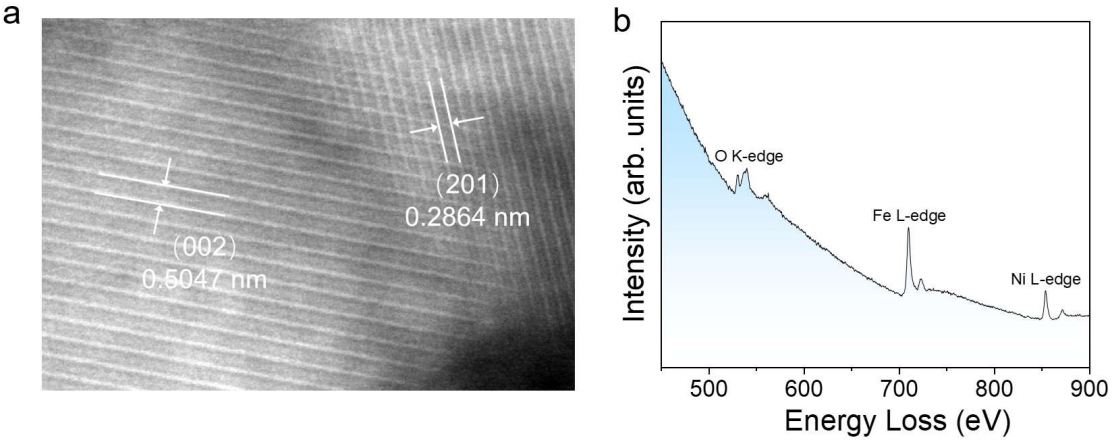

Figure S3. a) Ac-STEM image and b) EELS spectra of O K-edge, Fe L-edge and Ni-L edge for $NiFe(OH)_xCl_y$ powder.

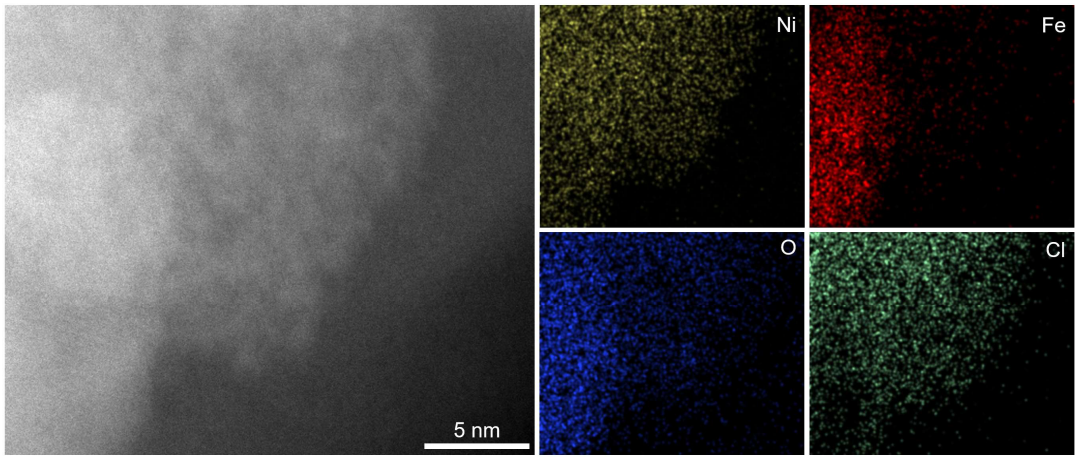

Figure S4. Ac-STEM image and EDS mapping of $NiFe(OH)_xCl_y$ for Ni, Fe, O, Cl elements.

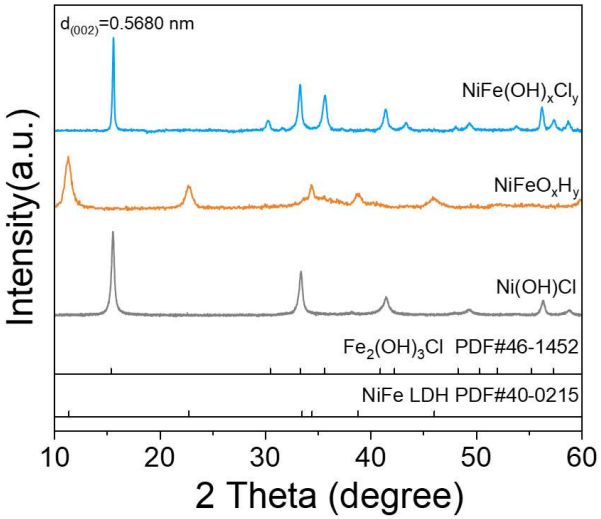

Figure S5. XRD pattern of $NiFe(OH)_xCl_y$, $NiFeO_xH_y$, Ni(OH)Cl powder and other phases.

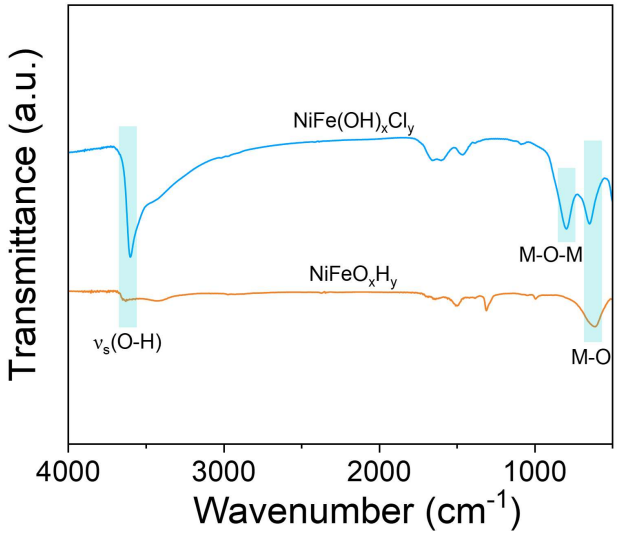

Figure S6. FTIR spectra of $NiFe(OH)_xCl_y$ and $NiFeO_xH_y$ powder.

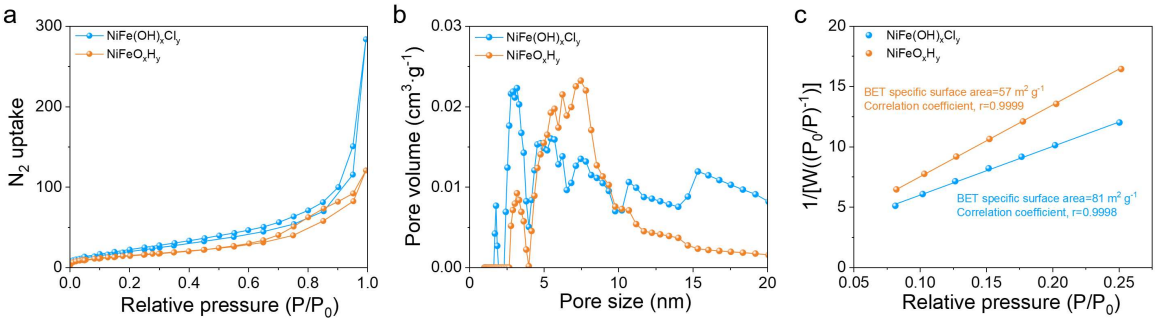

Figure S7. a) N_2 isothermal absorption and desorption curve, **b)** pore size distribution and **c)** BET surface area calculation of $NiFe(OH)_xCl_y$ and $NiFeO_xH_y$ powder.

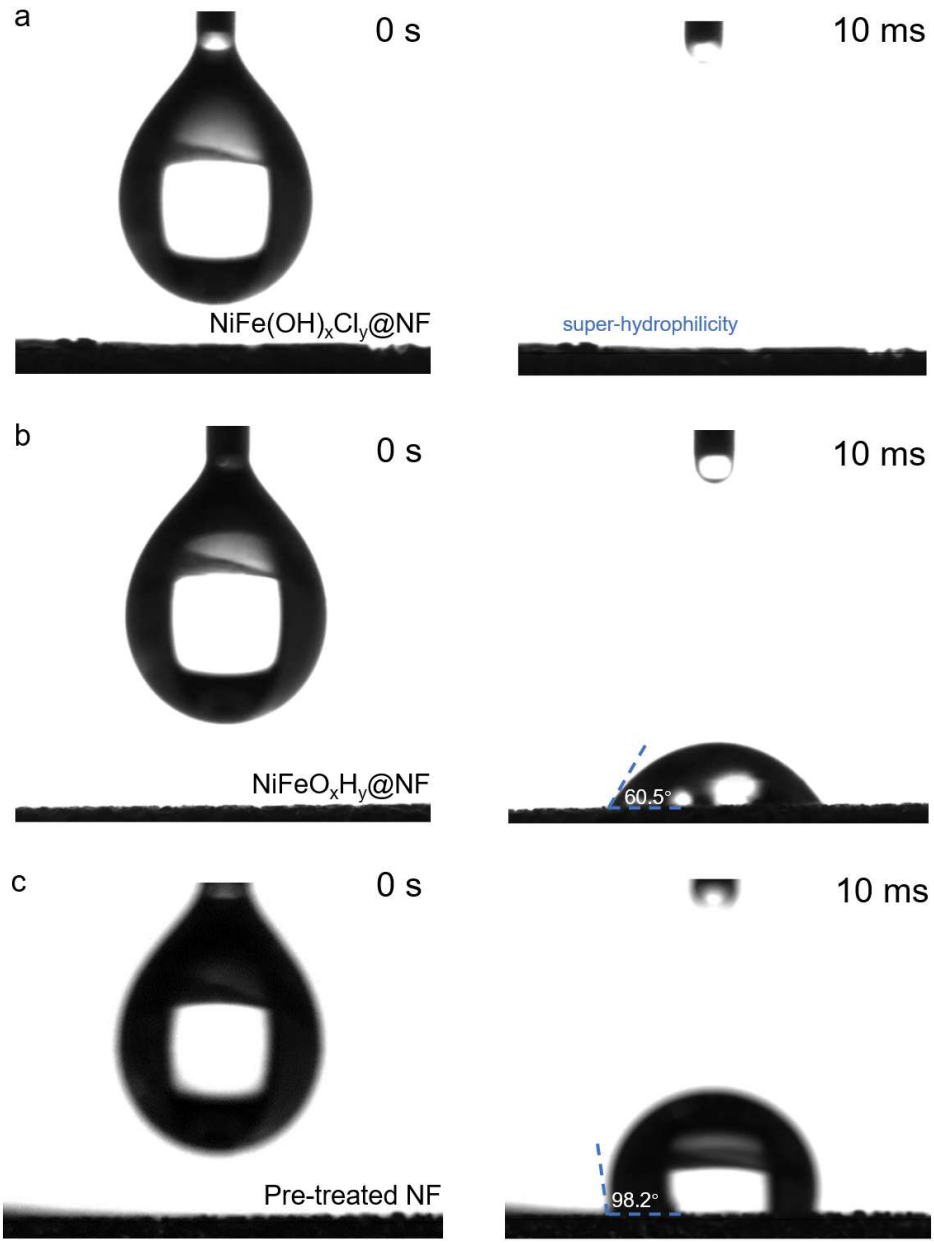

240

241 **Figure S8.** Contact angles of 1M KOH drop on a) $NiFe(OH)_xCl_y$@NF, b)

242 $NiFeO_xH_y$@NF and c pre-treated NF.

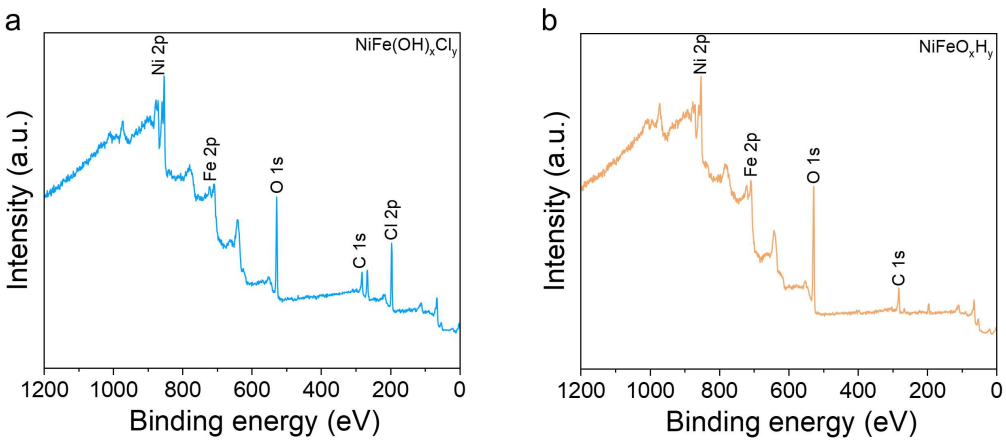

243

244 **Figure S9.** XPS surveys of a) $NiFe(OH)_xCl_y$ and b) $NiFeO_xH_y$.

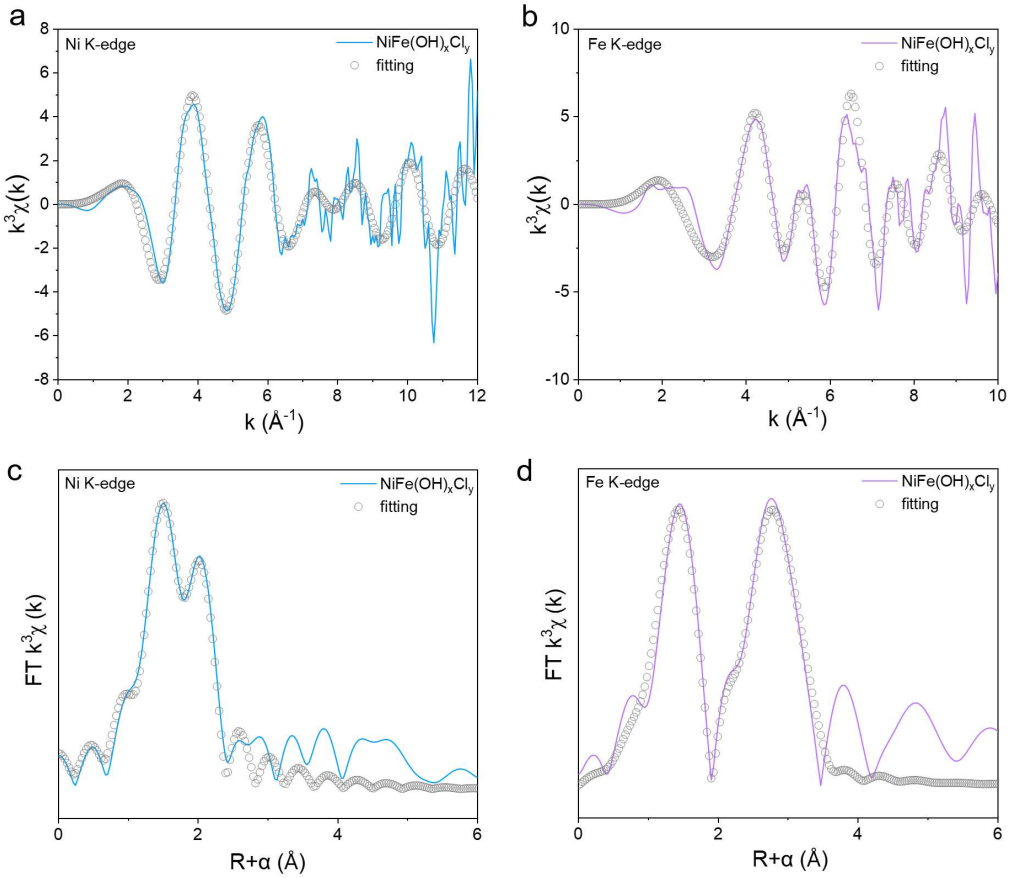

245

246 **Figure S10.** K^3-weighted χ (k) function oscillation and fitting curves of a) Ni K-edge

247 and b) Fe K-edge for $NiFe(OH)_xCl_y$. K^3-weighted χ (k) function of c) Ni K-edge and d)

248 Fe K-edge EXAFS spectra and fitting curves in the R space of $NiFe(OH)_xCl_y$.

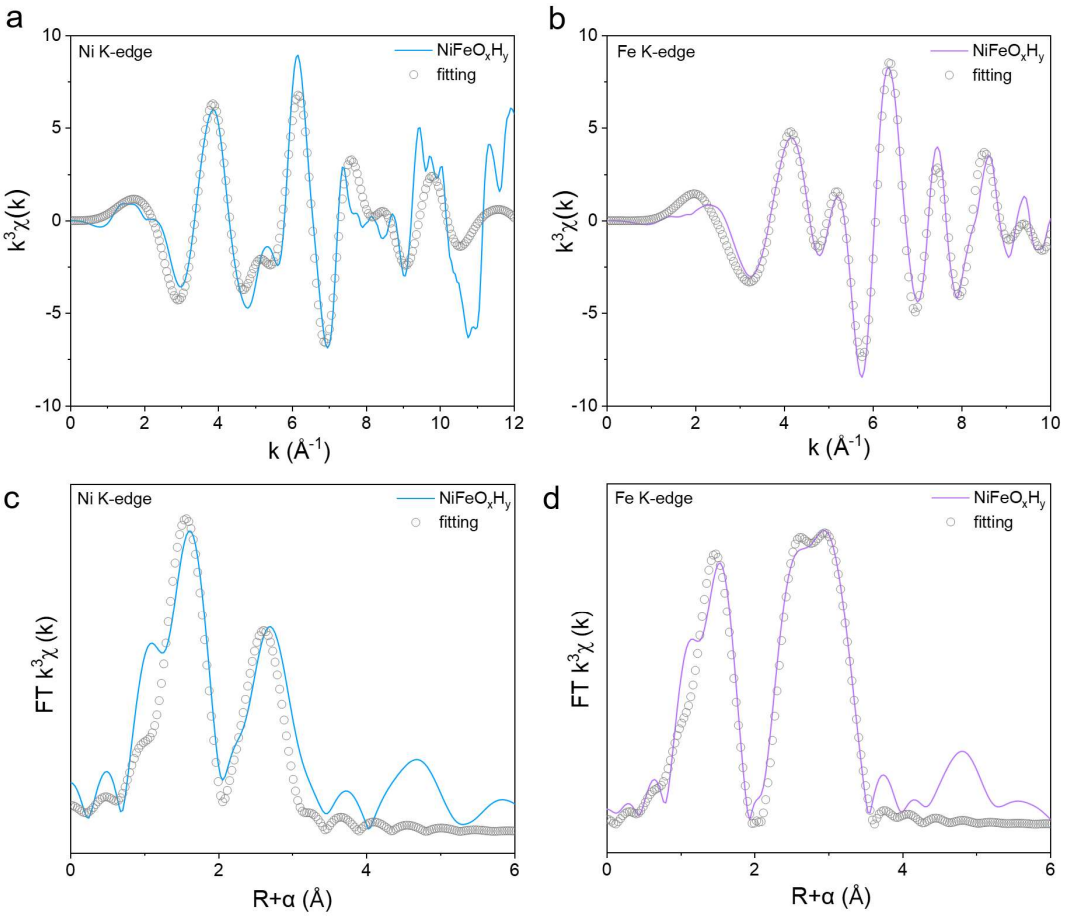

Figure S11. K^3-weighted χ (k) function oscillation and fitting curves of a) Ni K-edge and b) Fe K-edge for $NiFeO_xH_y$. K^3-weighted χ (k) function of c) Ni K-edge and d) Fe K-edge EXAFS spectra and fitting curves in the R space of $NiFeO_xH_y$.

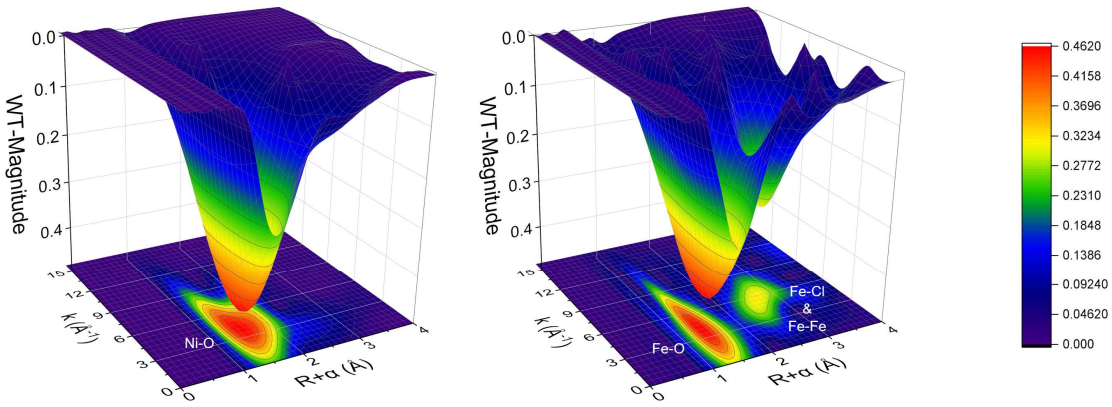

253

254 **Figure S12.** a) Ni-K edge and b) Fe K-edge WT-EXAFS spectra of $NiFe(OH)_xCl_y$.

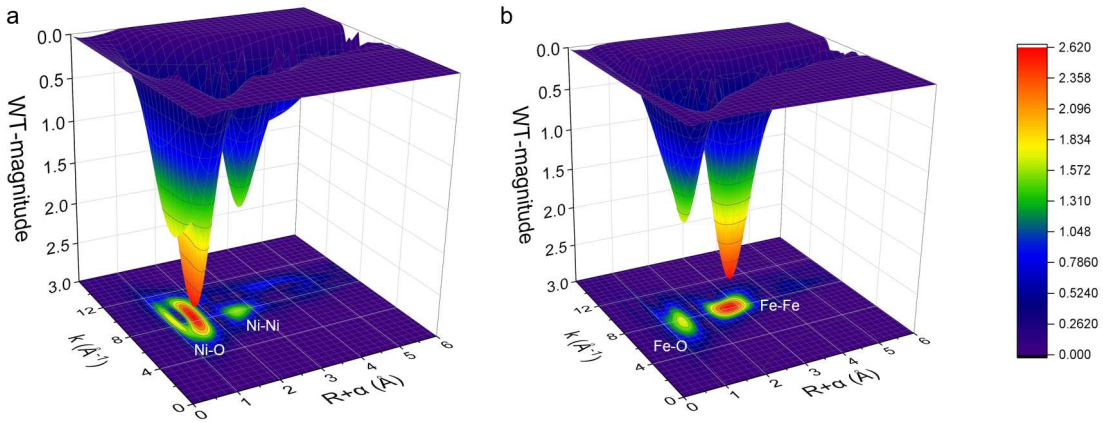

Figure S13. a) Ni-K edge and b) Fe K-edge WT-EXAFS spectra of $NiFeO_xH_y$.

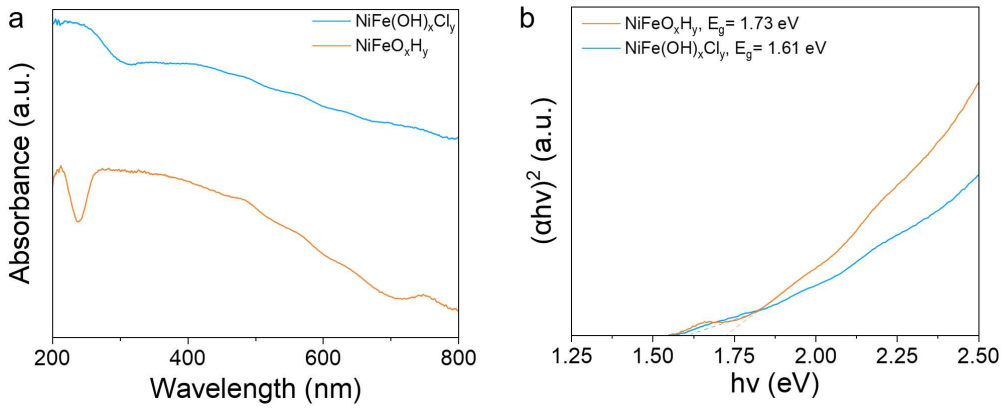

Figure S14. a) UV-Vis DRS spectra of $NiFe(OH)_xCl_y$ and $NiFeO_xH_y$. b) Tauc analyses of $NiFe(OH)_xCl_y$ and $NiFeO_xH_y$.

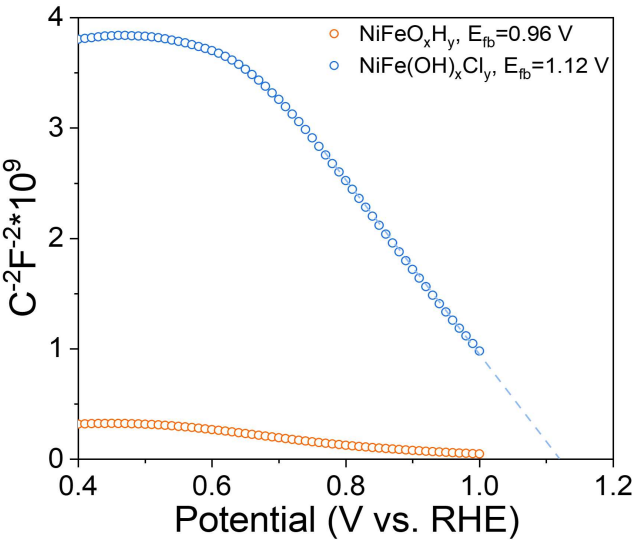

Figure S15. Mott-Schottky plots of $NiFe(OH)_xCl_y$ and $NiFeO_xH_y$.

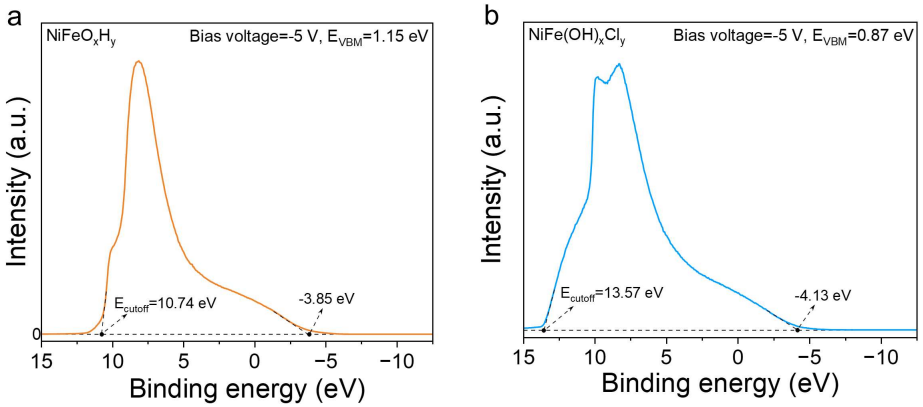

Figure S16. UPS spectra of a) $NiFeO_xH_y$ and b) $NiFe(OH)_xCl_y$.

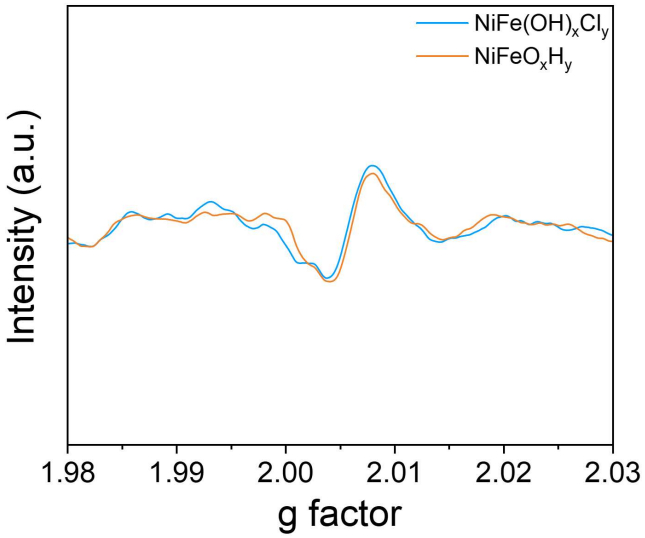

Figure S17. EPR spectra of $NiFe(OH)_xCl_y$ and $NiFeO_xH_y$.

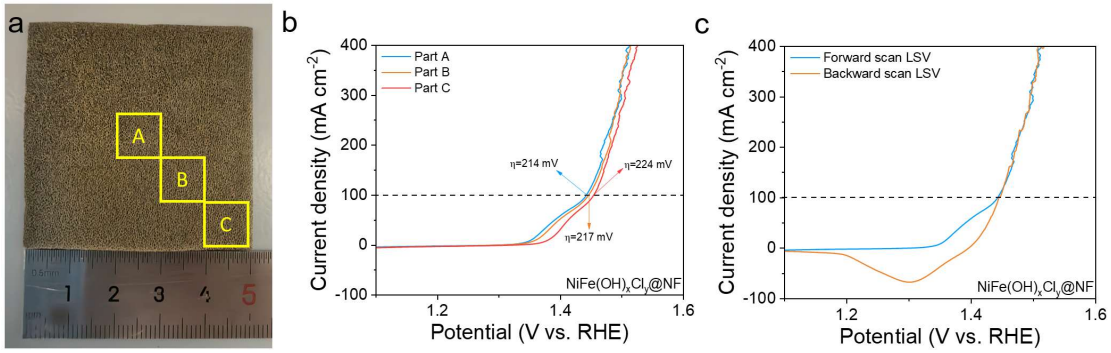

Figure S18. a) Schematic illustration of three different parts for the uniformity test. b) LSV curves of parts A, B and C with 95% iR compensation. c) Forward and backward scan LSV curves of $NiFe(OH)_xCl_y$@NF with 95% iR compensation

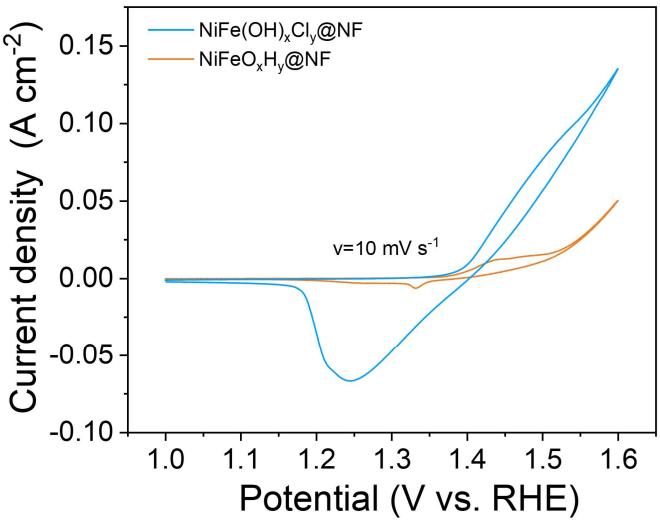

Figure S19. CV comparison of $NiFe(OH)_xCl_y$@NF and $NiFeO_xH_y$@NF.

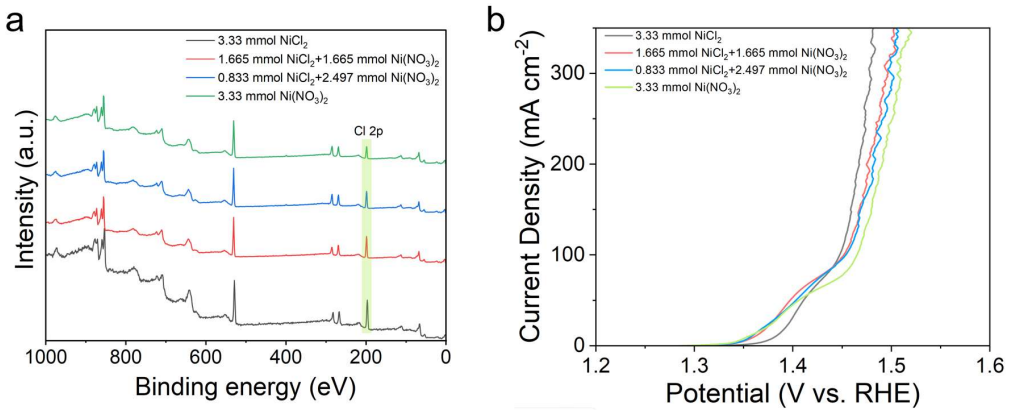

Figure S20. a) XPS survey of $NiFe(OH)_xCl_y$ powder with different constitutions of Ni salt. b) LSV curves of $NiFe(OH)_xCl_y$@NF with different Cl content.

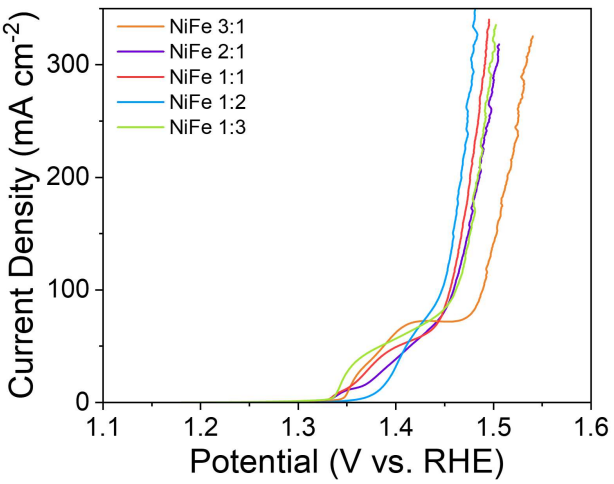

Figure S21. LSV curves of $NiFe(OH)_xCl_y$@NF with different Ni/Fe ratio.

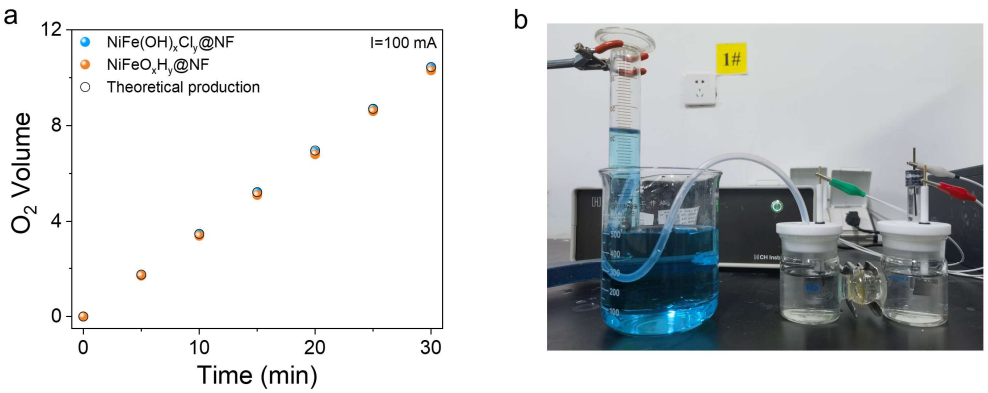

278

279 **Figure S22.** a) Faraday efficiency calculation of $NiFe(OH)_xCl_y$@NF and

280 $NiFeO_xH_y$@NF. b) Photo of the oxygen evolution test using the drainage method.

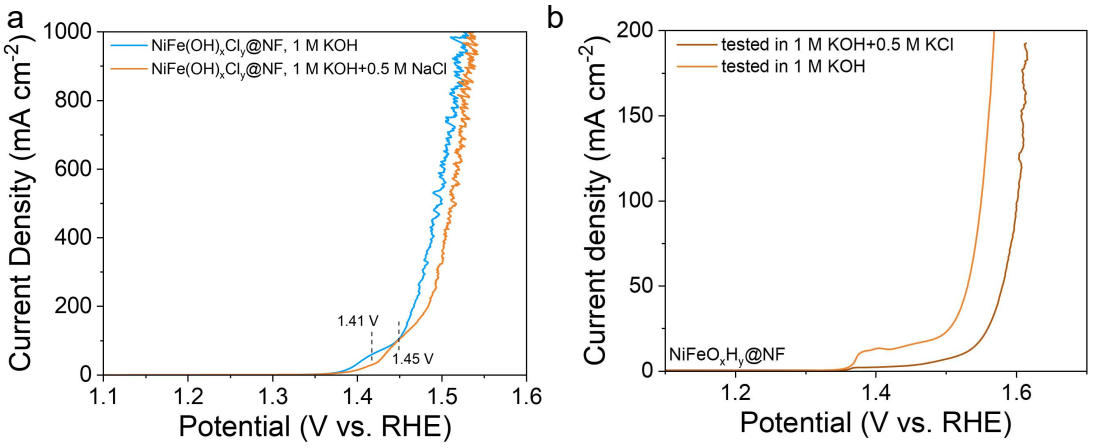

281

282 **Figure S23.** a) LSV curves of $NiFe(OH)_xCl_y$@NF in 1 M KOH and artificial seawater

283 (1 M KOH+0.5 M NaCl). b) LSV curves of $NiFeO_xH_y$@NF in 1 M KOH and 1 M

284 KOH+0.5 M KCl.

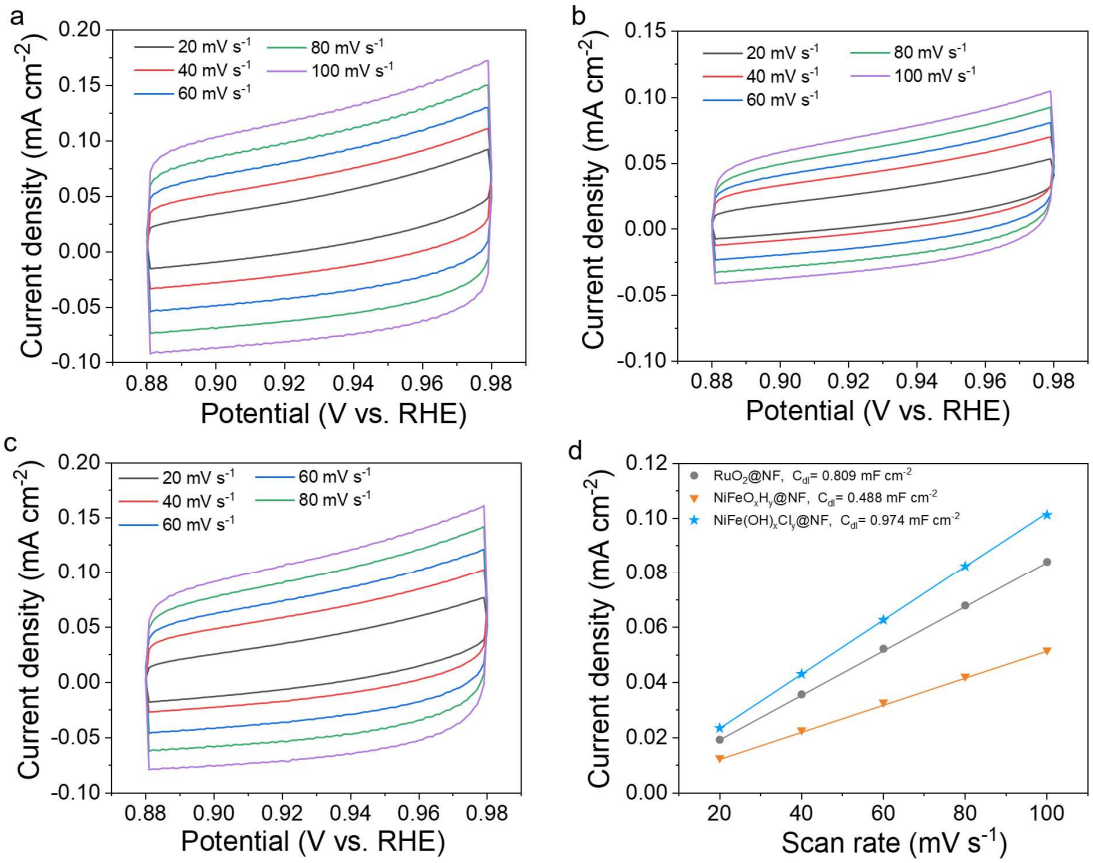

285

286 **Figure S24.** CV curves of a) $NiFe(OH)_xCl_y$@NF, b) $NiFeO_xH_y$@NF and c) RuO_2@NF

287 under non-Faradaic potential range. d) C_{dl} curves of $NiFe(OH)_xCl_y$@NF,

288 $NiFeO_xH_y$@NF and RuO_2@NF.

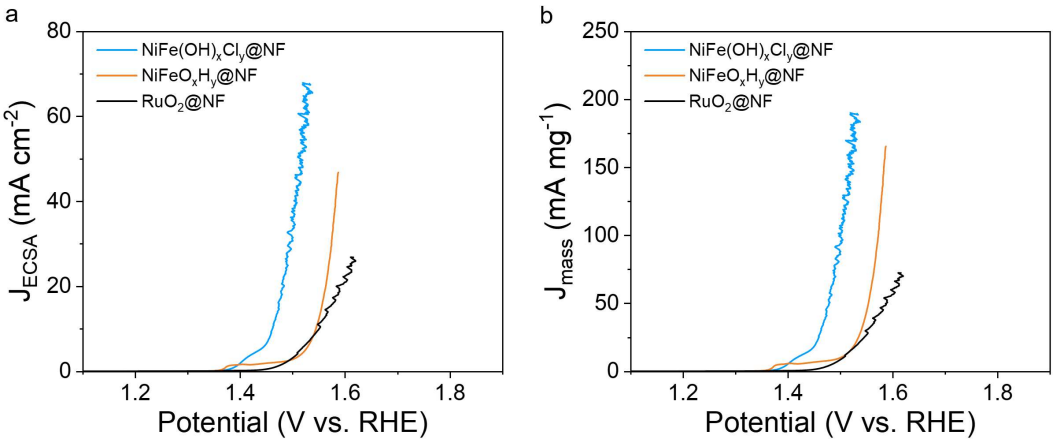

Figure S25. a) ECSA-normalized LSV curves and b) mass-normalized LSV curves of $NiFe(OH)_xCl_y$@NF, $NiFeO_xH_y$@NF and RuO_2@NF.

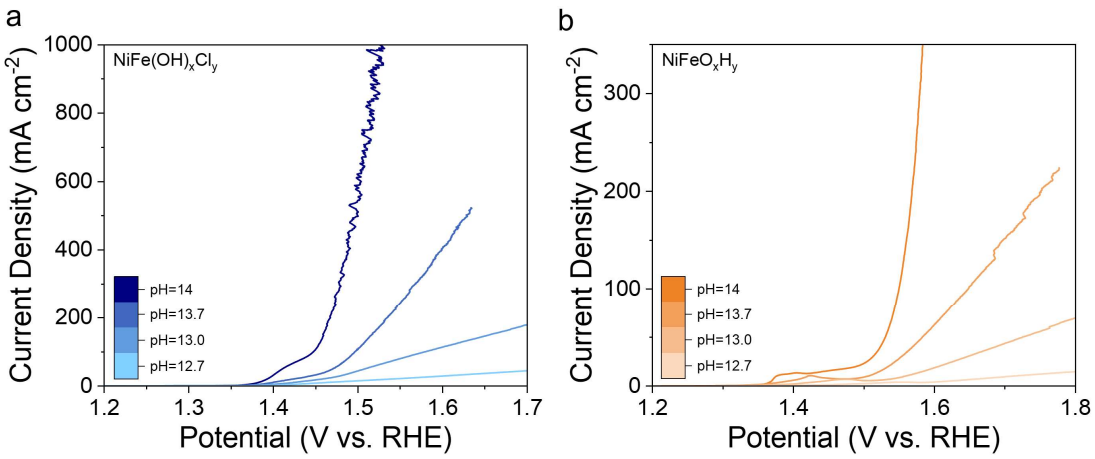

Figure S26. LSV curves of $NiFe(OH)_xCl_y$@NF and $NiFeO_xH_y$@NF in KOH electrolyte with different pH.

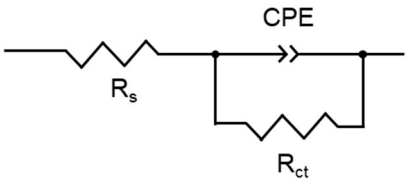

295

296 **Figure S27.** Fitting equivalent circuits of $NiFe(OH)_xCl_y$@NF and $NiFeO_xH_y$@NF.

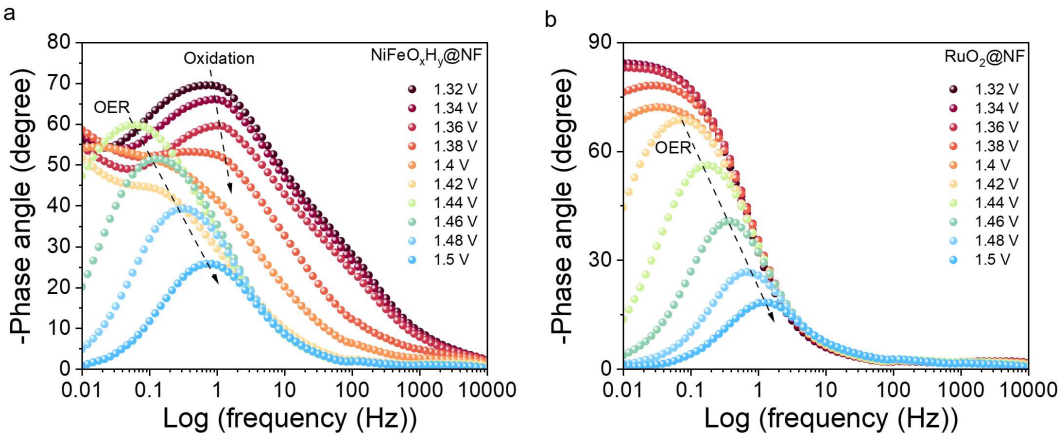

297

298 **Figure S28.** In-situ Bode plots of **a** $NiFeO_xH_y$@NF and **b** RuO_2@NF.

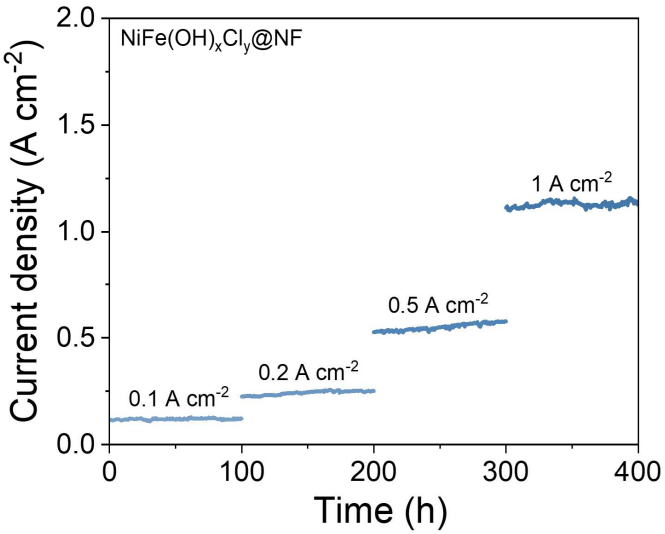

299

300 **Figure S29.** Step constant current test of $NiFe(OH)_xCl_y$@NF at various current

301 densities.

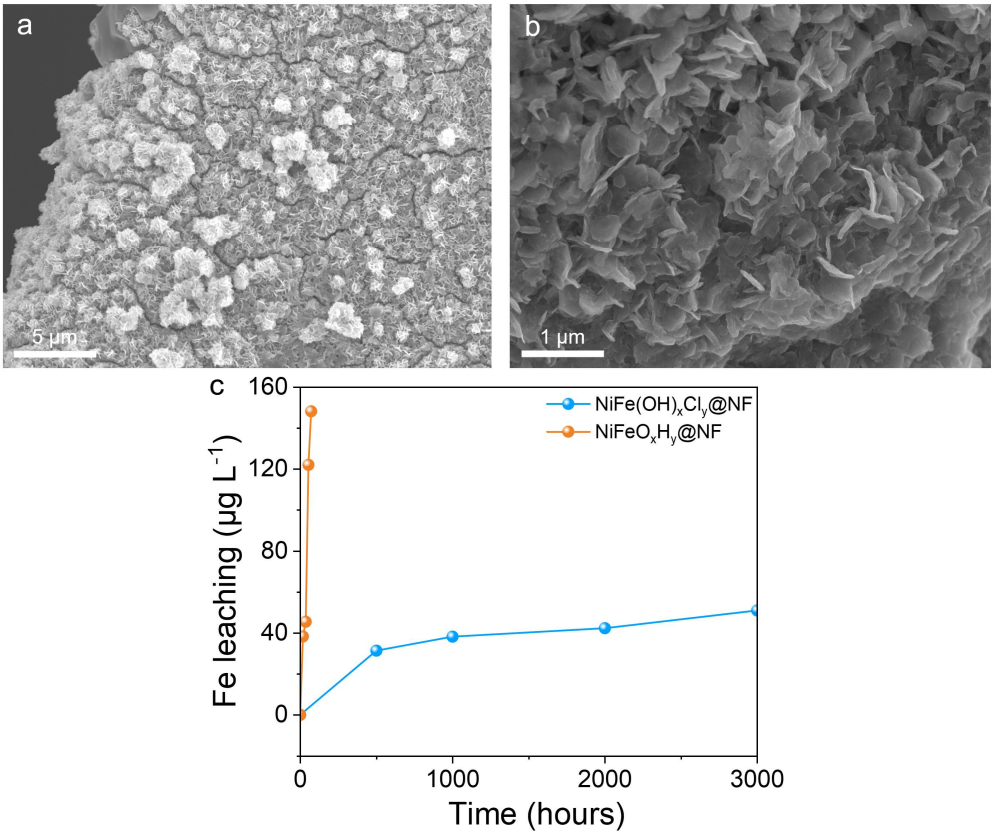

Figure S30. a-b) SEM images of $NiFe(OH)_xCl_y$@NF after 3000 h i-t test. c) ICP-MS results of Fe content in the electrolyte of $NiFe(OH)_xCl_y$@NF and $NiFeO_xH_y$@NF.

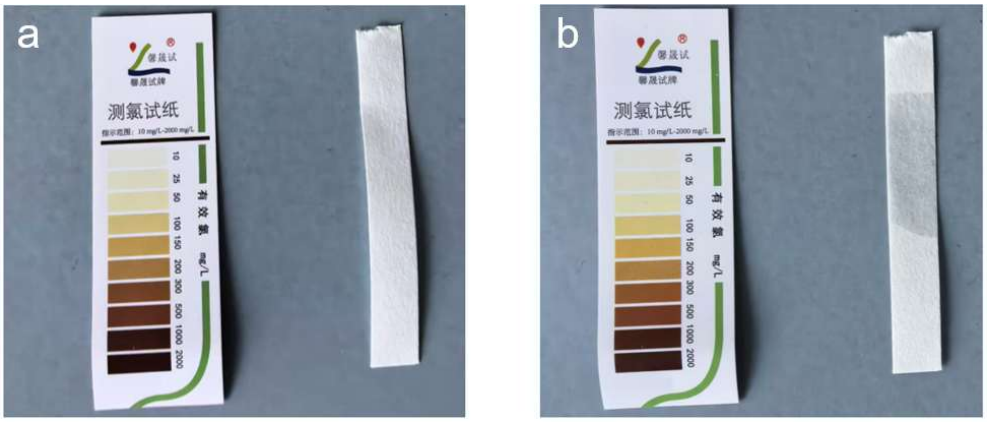

Figure S31. Chlorine test strips a) before and b) after dropping the tested electrolyte.

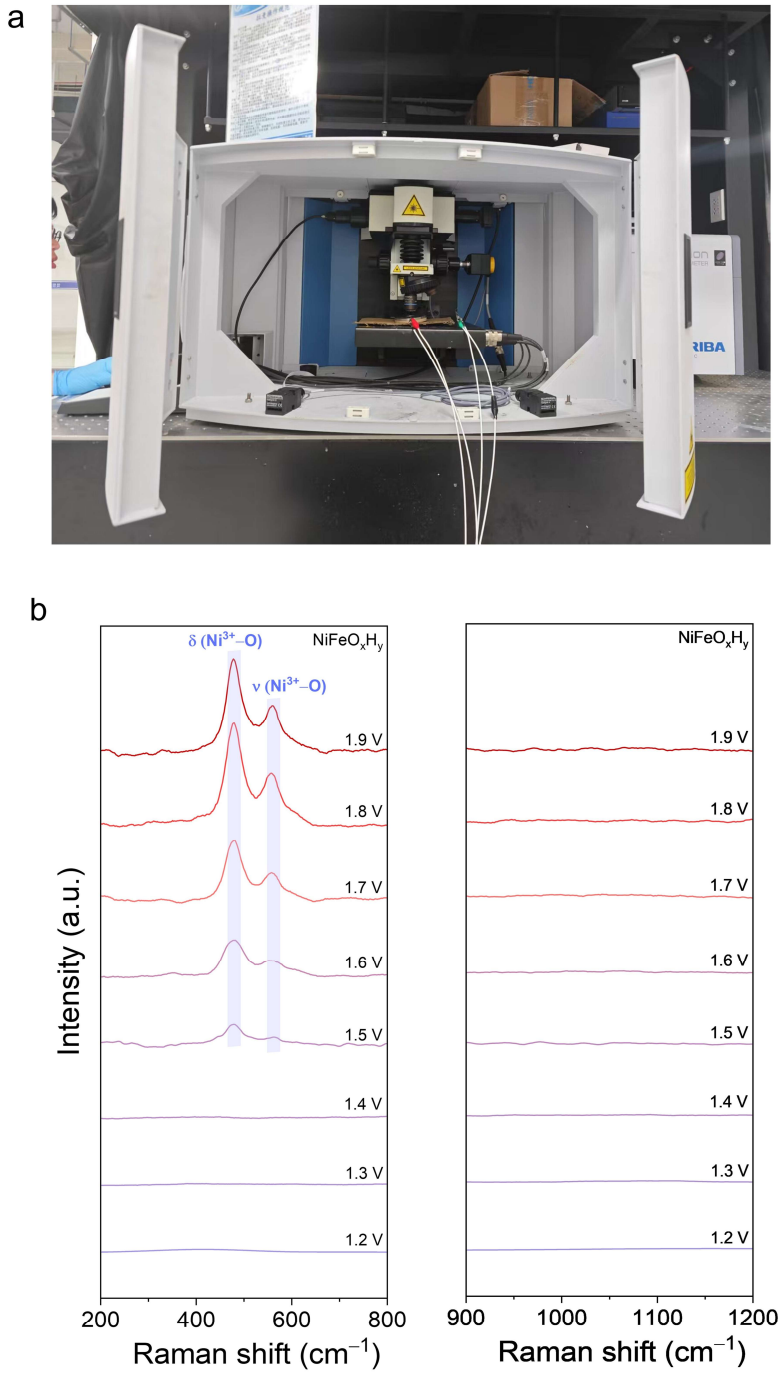

Figure S32. a) Picture of *Operando* Raman test. b) *Operando* Raman spectra of $NiFeO_xH_y$.

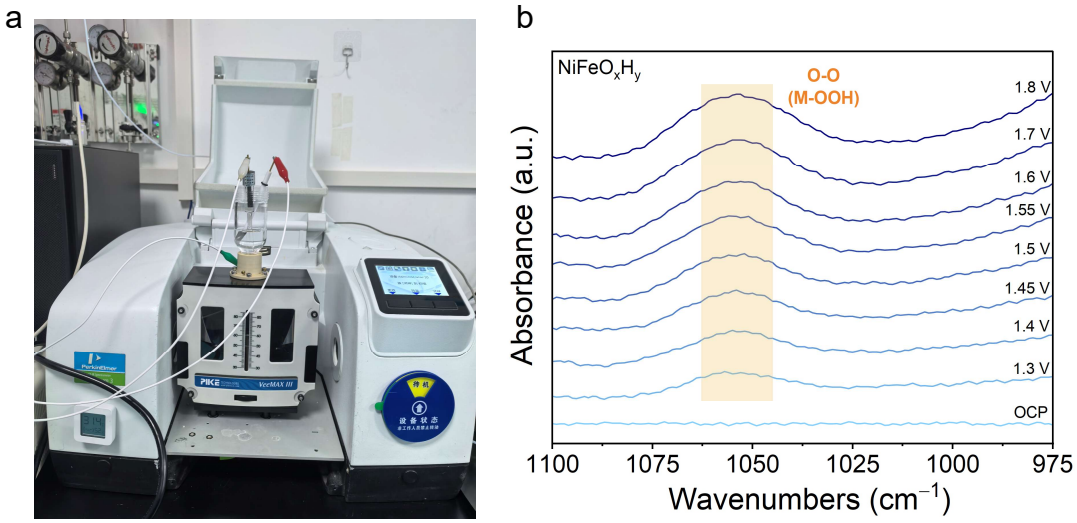

312

313 **Figure S33.** a) Picture of *Operando* ATR-FTIR test. b) *Operando* ATR-FTIR spectra

314 of $NiFeO_xH_y$.

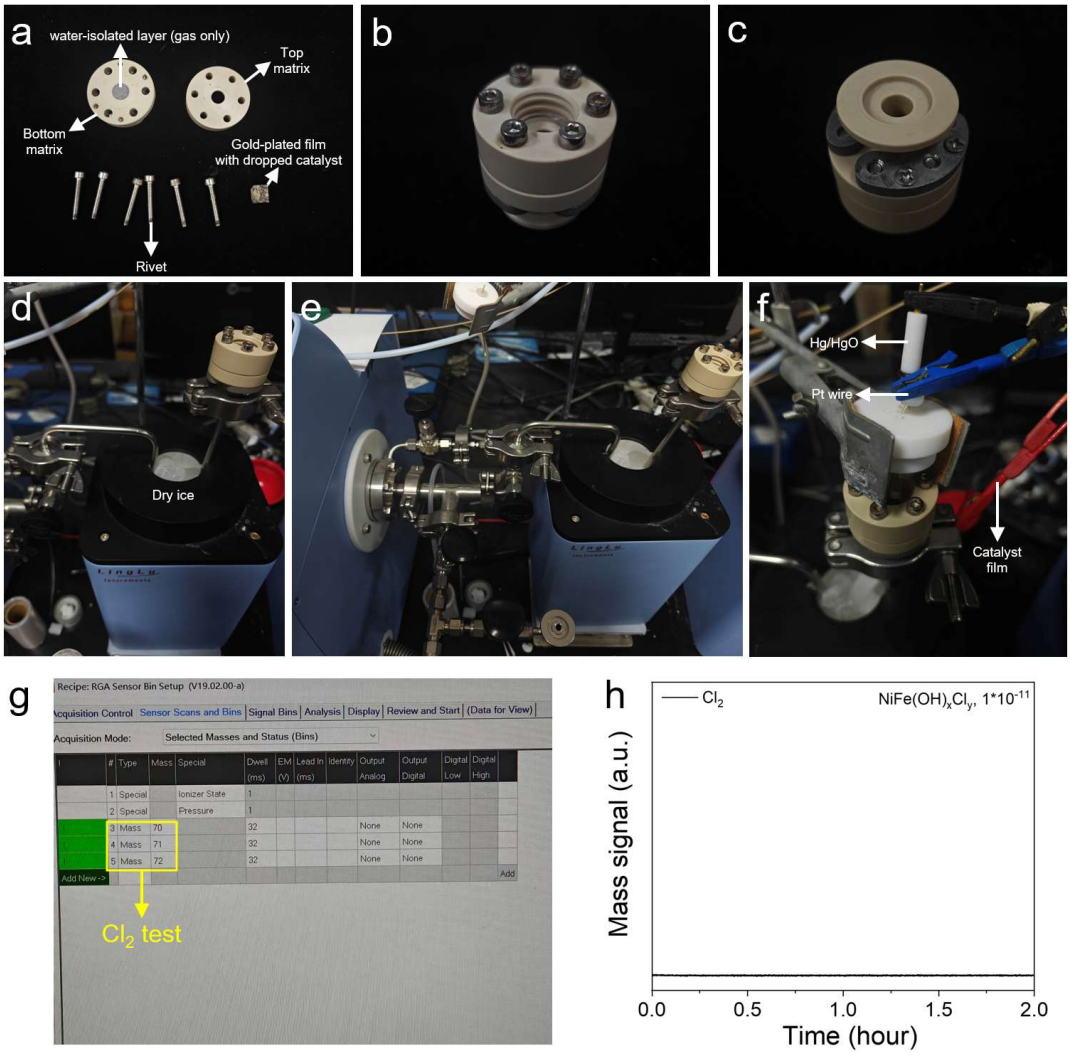

Figure S34. a) Schematic picture of the individual components of the DEMS cell. b) Top matrix and c) bottom matrix of the DEMS cell. d) Schematic picture of dry-ice condensation. e) Schematic diagram of the connection between the *operando* electrochemical setup and the mass spectrometer. f) Three-electrode *operando* electrochemical setup. g) Parameter settings for the detection of target gas molecular masses (m/z channels). h) *Operando* DEMS Cl_2 signals measurement during LSV process of $NiFe(OH)_xCl_y$.

As shown in Figure S31a, the DEMS cell consists of an upper and a lower module. The lower module contains a hydrophobic water-separation membrane, which blocks liquid permeation while allowing the evolved gases to pass through. The two modules are fastened by multiple rivets, and a catalyst-coated gold-plated membrane is sandwiched between them. Figure S34b and Figure S34c show the upper and lower

modules of the cell, respectively. The gases generated during OER were directed to a dry-ice trap for condensation and separation; during analysis, the condensates were re-vaporized and introduced into the mass spectrometer for detection (Figure S34d–e). The OER was conducted in a three-electrode configuration, using Hg/HgO as the reference electrode, a Pt wire as the counter electrode, and the catalyst-loaded gold-plated membrane as the working electrode (Figure S34f). Before gas collection, the target mass-to-charge (m/z) channels were preset (e.g., m/z=70, 71, and 72 for Cl_2, Figure S34g). Notably, for chlorine detection, continuous cyclic scans were performed between 0.076 and 0.676 V (1.0–1.6 V vs RHE) at 5 mV s^{-1} for 60 cycles (120 min), and the Cl_2 evolution signal was monitored throughout the entire process.

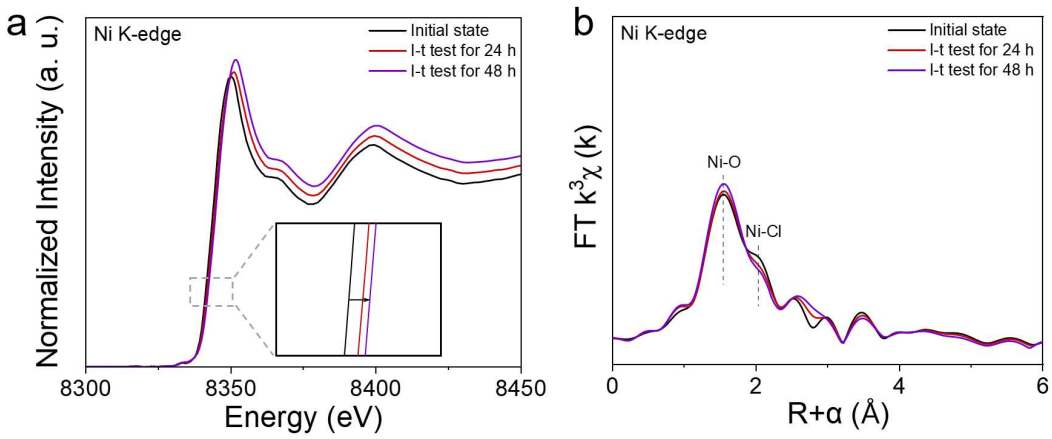

338

339 **Figure S35.** a) Ni K-edge in situ XANES spectra of $NiFe(OH)_xCl_y$. b) K^3-weighted χ

340 (k) function of Ni K-edge in situ EXAFS spectra in the R space.

341

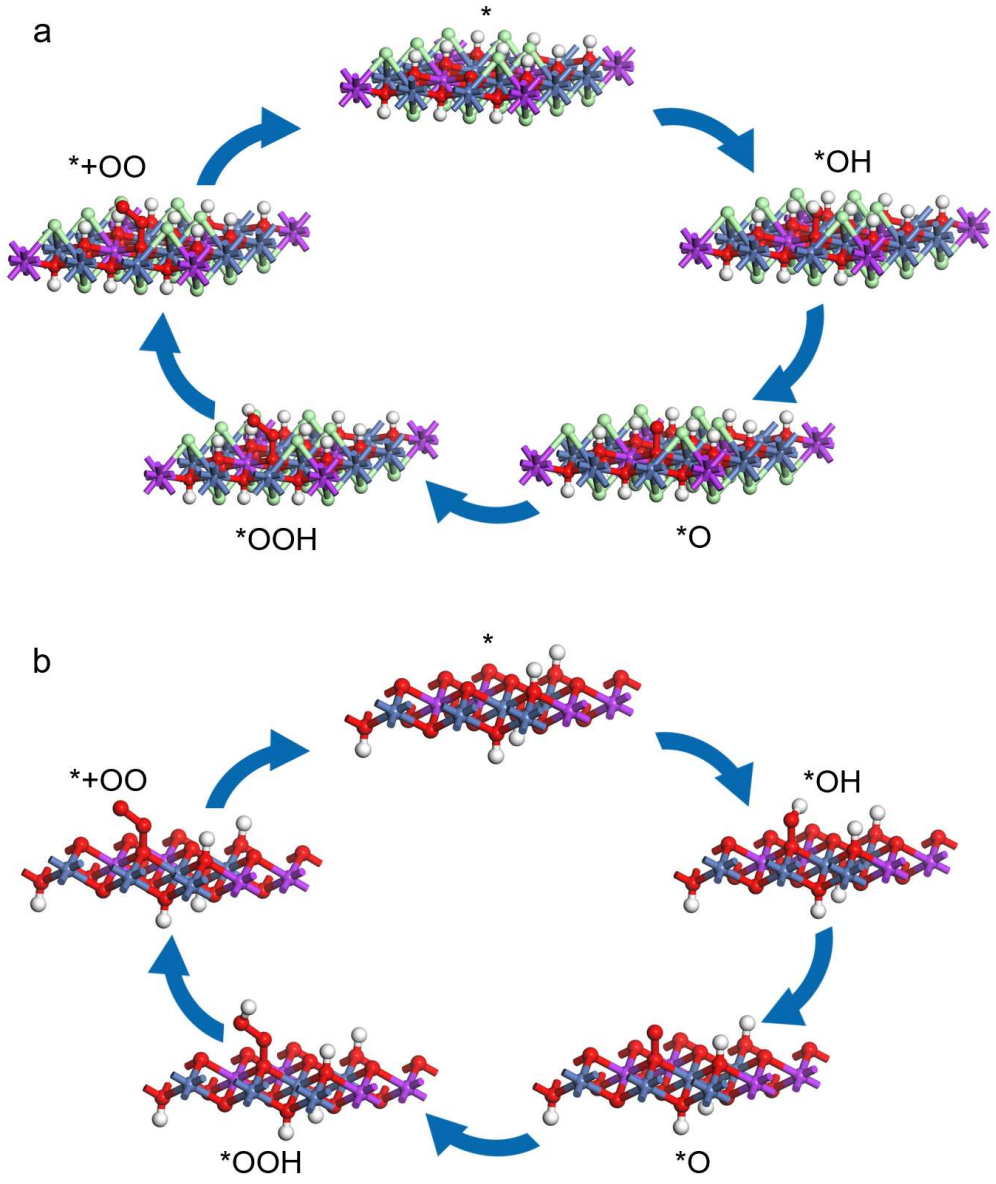

Figure S36. Calculation models of a $NiFe(OH)_xCl_y$ and b $NiFeO_xH_y$ in AEM pathway.

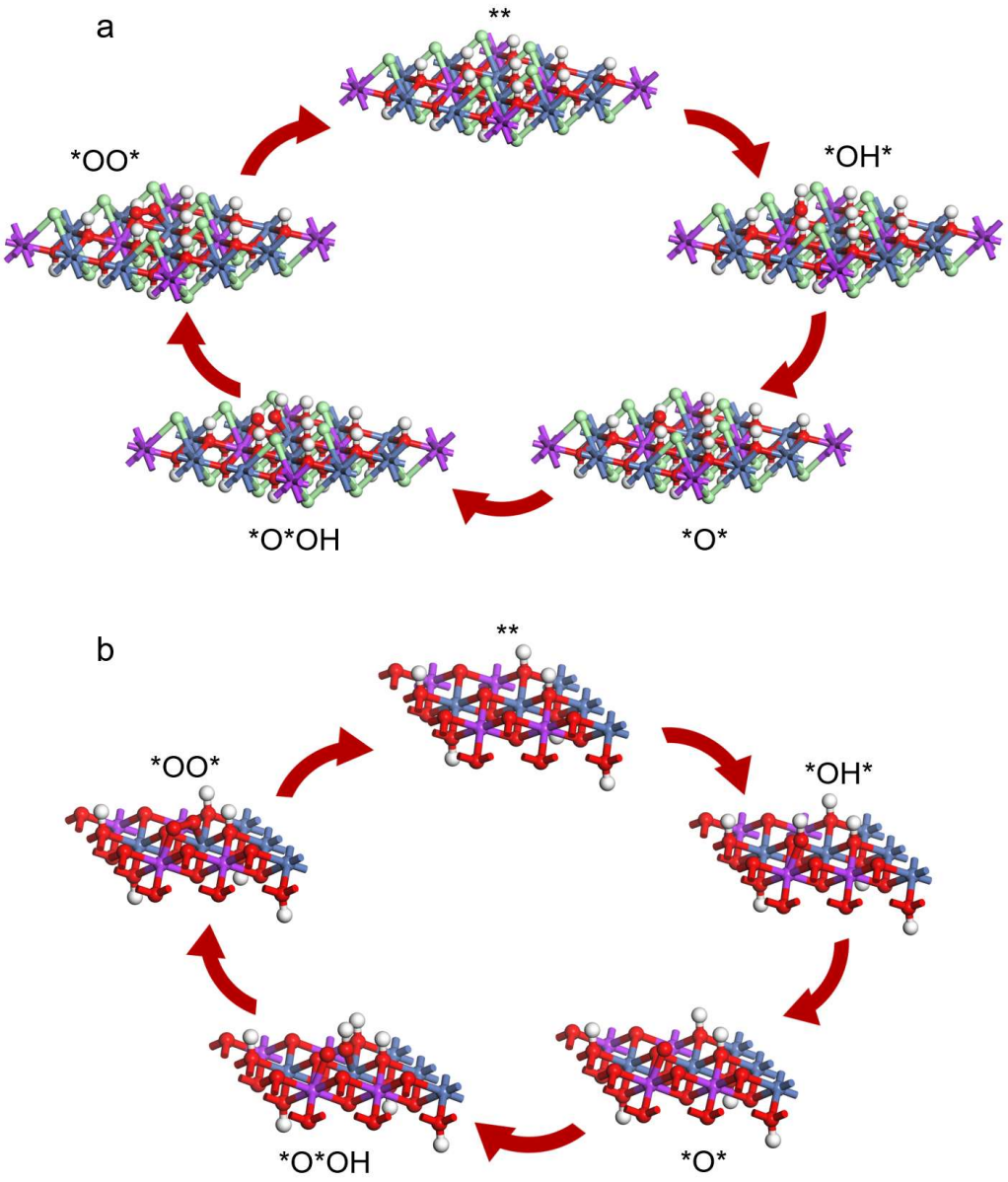

Figure S37. Calculation models of a $NiFe(OH)_xCl_y$ and b $NiFeO_xH_y$ in OPM pathway.

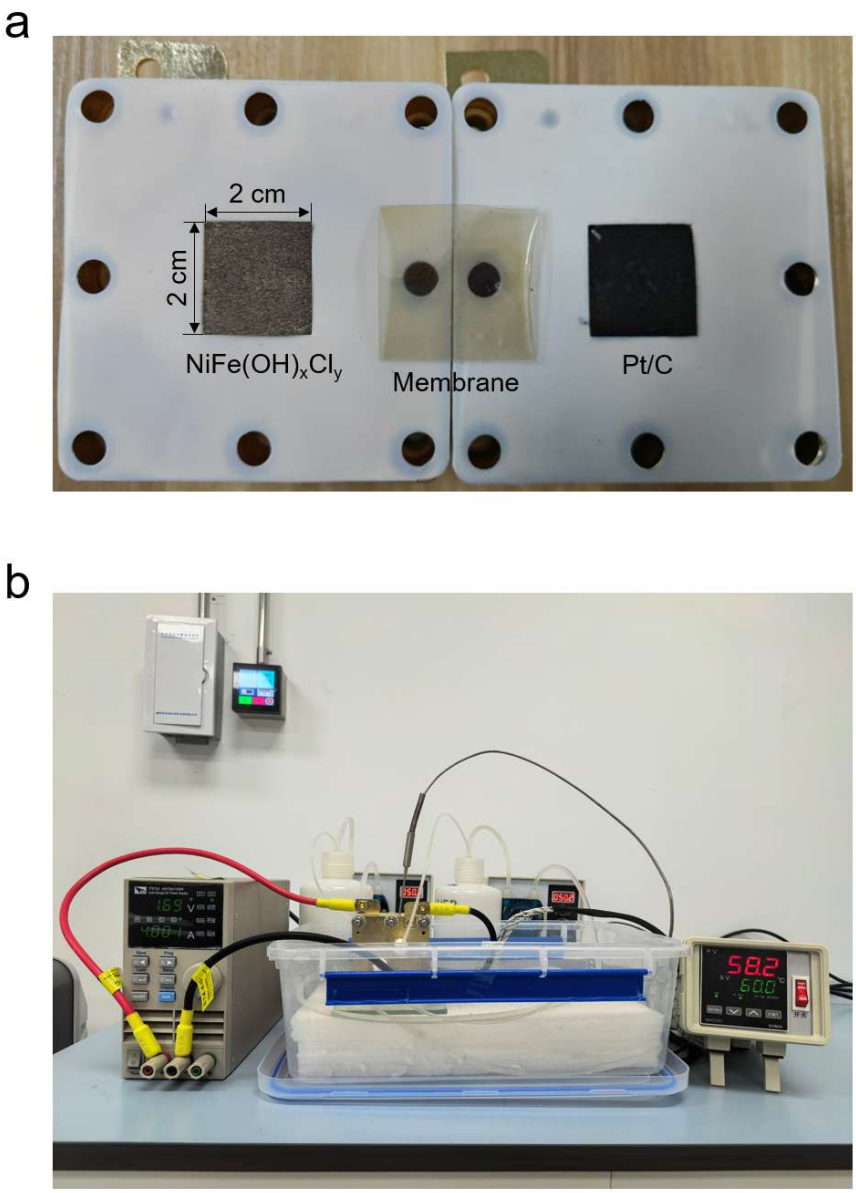

Figure S38. a) Compositions of $NiFe(OH)_xCl_y$‖Pt/C AEMWE. b) Assembled $NiFe(OH)_xCl_y$‖Pt/C AEMWE (2×2 cm^2) tested at 1 A cm^{-2}, 1.69 V.

Notes: The energy efficiency of the AEMWE was evaluated based on the ratio between the thermoneutral voltage and the actual operating voltage. The thermoneutral voltage of water electrolysis under standard conditions is considered to be 1.48 V, which accounts for both the Gibbs free energy and the enthalpy change (i.e., the total energy input required to produce H_2 and O_2 without heat exchange). Accordingly, the voltage efficiency (η) was calculated as:

$$\eta = 1.48/U_{cell} \quad (1)$$

where U_{cell} is the actual operating voltage of the electrolyzer. The theoretical electric charge required to produce 1 kg of hydrogen was calculated based on Faraday's law and the molecular weight of hydrogen gas. The molar mass of H_2 is 2.016 g mol^{-1}, thus 1 kg of H_2 corresponds to:

$$n_{H2}=1000/2.16=496 \text{ mol} \quad (2)$$

The total charge required for producing 496 mol of H_2 is:

$$Q=2\times96485\times196=9.57\times10^7 \text{ C} \quad (3)$$

The corresponding electrical energy input is calculated as:

$$E= Q\times U_{cell}/3600\times1000 \text{ (kWh)} \quad (4)$$

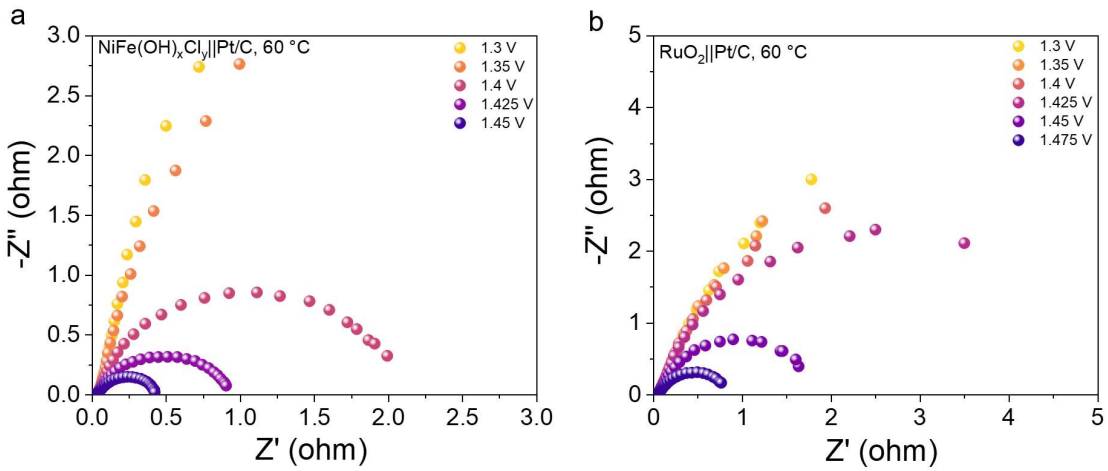

366

367 **Figure S39.** In-situ EIS plots of a) $NiFe(OH)_xCl_y$‖Pt/C and b) $NiFeO_xH_y$‖Pt/C at 60 °C.

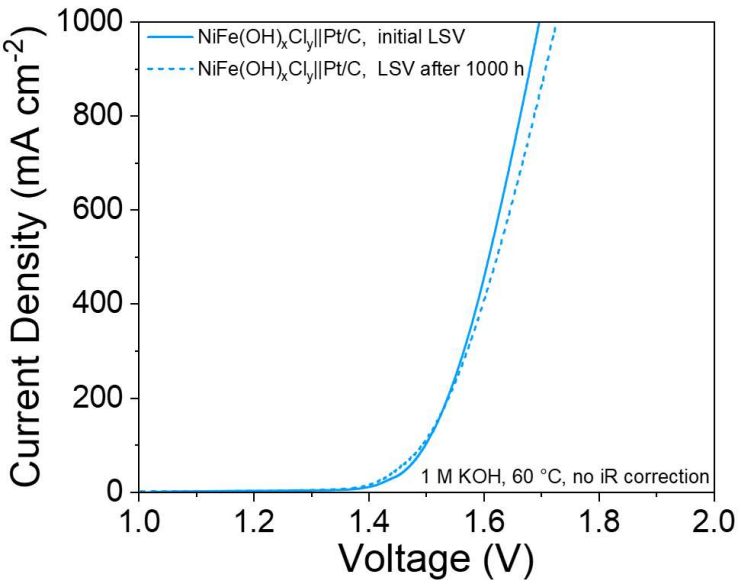

Figure S40. LSV curves of $NiFe(OH)_xCl_y$||Pt/C at 60 ℃ before and after 1000 h i-t test without iR compensation.

Table S1. EDS results of $NiFe(OH)_xCl_y$ and $NiFeO_xH_y$ from SEM mapping.

$NiFe(OH)_xCl_y$:

Element	Line type	Apparent concentration	k ratio	wt.%
C	k linear system	2.49	0.02493	6.69
O	k linear system	53.61	0.18040	16.69
Cl	k linear system	46.58	0.40709	21.59
Fe	k linear system	28.98	0.28976	14.64
Ni	k linear system	72.23	0.72226	40.40

$NiFeO_xH_y$:

Element	Line type	Apparent concentration	k ratio	wt.%
C	k linear system	1.93	0.01933	3.80
O	k linear system	69.69	0.27250	27.27
Fe	k linear system	36.29	0.36290	27.46
Ni	k linear system	51.50	0.51498	40.83

Table S2. XPS ratio of Ni^{2+}/Ni^{3+} and Fe^{2+}/Fe^{3+} for $NiFe(OH)_xCl_y$ and $NiFeO_xH_y$.

$NiFe(OH)_xCl_y$:

valence \ element	Ni 2p 3/2	Ni 2p 1/2	Fe 2p 3/2	Fe 2p 1/2
+2	68.9%	69.0%	43.3%	43.1%
+3	31.1%	31.0%	56.7%	56.9%

$NiFeO_xH_y$:

valence \ element	Ni 2p 3/2	Ni 2p 1/2	Fe 2p 3/2	Fe 2p 1/2
+2	66.6%	66.9%	48.5%	48.2%
+3	33.4%	33.1%	51.5%	51.8%

Table S3. EXAFS fitting parameters at the Ni K-edge for various samples (S_0^2=0.82 from Ni-foil).

[a]*CN*: coordination numbers; [b]*R*: bond distance; [c]σ^2: Debye-Waller factors; [d] ΔE_0: the inner potential correction. R factor: goodness of fit. Error bounds that characterize the

	shell	CN[a]	R[b] (Å)	σ^{2c} (Å^2)	ΔE_0[d] (eV)	R factor
Ni-foil	Ni-Ni	12	2.47±0.01	0.0062	6.2±1.1	0.0049
$NiFe(OH)_xCl_y$	Ni-O	4.8±0.3	2.04±0.01	0.0088	-3.4±1.3	0.0112
	Ni-Cl	1.6±0.2	2.41±0.01	0.0045		
$NiFeO_xH_y$	Ni-O	5.1±0.3	2.04±0.01	0.0089	-2.6±1.0	0.0182
	Ni-Ni	8.6±0.2	3.01±0.02	0.0091		

structural parameters obtained by EXAFS spectroscopy were estimated as CN±20%; R±1%; σ^2±20%.

Table S4. EXAFS fitting parameters at the Fe K-edge for various samples S_0^2=0.80 from Fe-foil）

	shell	CN[a]	R[b] (Å)	σ^{2c} (Å^2)	ΔE_0[d] (eV)	R factor
Fe-foil	Fe-Fe1	8	2.47±0.01	0.0045	6.2±1.4	0.0032
	Fe-Fe2	6	2.85±0.01	0.0057		
$NiFe(OH)_xCl_y$	Fe-O	3.4±0.2	1.97±0.01	0.0095	2.3±1.1	0.0052
	Fe-Cl	1.0±0.2	2.48±0.01	0.0110		
	Fe-Fe1	2.9±0.4	2.97±0.01	0.0120		
	Fe-Fe2	4.6±0.7	3.45±0.01	0.0130		
$NiFeO_xH_y$	Fe-O	4.2±0.2	1.94±0.01	0.0096	-4.3±1.2	0.0072
	Fe-Fe1	3.4±0.2	2.96±0.01	0.0110		
	Fe-Fe2	7.2±0.3	3.45±0.01	0.0120		

[a]*CN*: coordination numbers; [b]*R*: bond distance; [c]σ^2: Debye-Waller factors; [d]ΔE_0: the inner potential correction. R factor: goodness of fit. Error bounds that characterize the structural parameters obtained by EXAFS spectroscopy were estimated as CN±20%; R±1%; σ^2±20%.

393 **Table S5**. Elemental ratio of $NiFe(OH)_xCl_y$ synthesized with different constitutions of

394 Ni salt.

Ni salts constitution \ elemental ratio (at.%)	Ni	Fe	O	**Cl**
3.33 mmol $NiCl_2$	24.0%	13.4%	38.3%	**24.3%**
1.665 mmol $NiCl_2$+1.665 mmol $Ni(NO_3)_2$	23.7%	12.1%	45.6%	**18.6%**
0.833 mmol $NiCl_2$+2.499 mmol $Ni(NO_3)_2$	24.0%	13.4%	47.2%	**15.4%**
3.33 mmol $Ni(NO_3)_2$	26.2%	13.6%	47.9%	**12.3%**

395

Table S6. C_{dl} and ECSA of $NiFe(OH)_xCl_y$@NF, $NiFeO_xH_y$@NF and commercial RuO_2@NF (Assuming the standard specific non-faradaic capacitance Cs=60 μF cm^{-2}).

	C_{dl} (mF cm^{-2})	ECSA (cm^2)
$NiFe(OH)_xCl_y$ @NF	0.974	16.23
$NiFeO_xH_y$@NF	0.488	8.13
RuO_2@NF	0.809	13.48

Table S7. Comparison of OER performance among recently reported Ni/Fe-based catalysts in alkaline media.

Catalysts	Overpotential at 100 mA cm^{-2} (mV)	Tafel slope (mV dec^{-1})	Stability (hours@ current density)	Ref.
$NiFe(OH)_xCl_y$@NF	**217**	**39.6**	**3000 h@1 A cm^{-2}**	**This work**
NiFe-SQ/NF-R	225	50	700 h@3 A cm^{-2}	***Nat. Commun.*** 2025, 16, 3407
R-NiFeOOH@SO_4	251	56	150 h@0.5 A cm^{-2}	***Nat. Commun.*** 2024, 15, 8293
CoNi-PI	282	42	48 h@0.1 A cm^{-2}	***J. Am. Chem. Soc.*** 2025, 147, 13928−13936
$V_{Cr,Co}$-NiFeOOH	239	39.5	500 h@0.5 A cm^{-2}	***J. Am. Chem. Soc.*** 2025, 147, 3, 2607–2615
NiCoFeCrMnS-HES	235	40.5	100 h@0.1 A cm^{-2}	***Adv. Mater.*** 2025, 2508610
NiFe(S)/NM	290	41.4	500 h@0.3 A cm^{-2}	***Angew. Chem. Int. Ed.*** 2025, 64, e202500303
NiFe-LDH/Ni_4Mo	260	42	60 h@0.1 A cm^{-2}	***Angew. Chem. Int. Ed.*** 2025, 64, e202413250
$Ni_2Fe_1Co_{0.75}$	350	48.9	2 h@0.1 A cm^{-2}	***Adv. Energy Mater.*** 2024, 2400029
Ru-S-NiFe LDH	279	81.6	100 h@0.25 A cm^{-2}	***Adv. Energy Mater.*** 2025, 2500554
NiFeS	248	36.3	100 h@0.35 A cm^{-2}	***Adv. Funct. Mater.*** 2025, 2506656
NFMN-FeOOH	295	40	300 h@0.5 A cm^{-2}	***Adv. Funct. Mater.*** 2023, 2311854
$(NiFeCoMn)_3S_4$	410	75.6	48 h@0.01 A cm^{-2}	***Adv. Funct. Mater.*** 2023, 33, 2208170
NC-$CoNi_2S_4$@ReS_2/CC	300	54.7	60 h@0.1 A cm^{-2}	***Adv. Sci.*** 2025, 12, 2413245
NiFe-LDH-PTA	230	83.3	500 h@1 A cm^{-2}	***ACS Catal.*** 2025, 15, 8, 6486–6496
H-FeCoS/NC-0.50	330	81.3	30 h@0.01 A cm^{-2}	***Appl. Catal. B*** 2024, 359, 124530

Table S8. Calculated Gibbs free energy variation of NiFe(OH)Cl and $NiFeO_xH_y$ in AEM pathway.

	$NiFe(OH)_xCl_y$ (eV, U=0 V)	$NiFe(OH)_xCl_y$ (eV, U=1.23 V)	$NiFeO_xH_y$ (eV, U=0 V)	$NiFeO_xH_y$ (eV, U=1.23 V)
*	0	0	0	0
*OH	1.00951	-0.13491	1.17103	-0.05897
*O	1.68916	-0.77084	2.34441	-0.11559
*OOH	3.19612	-0.49388	2.90893	-0.78107
*+O_2	4.92	0	4.92	0

Table S9. Calculated Gibbs free energy variation of NiFe(OH)Cl and $NiFeO_xH_y$ in OPM pathway.

	$NiFe(OH)_xCl_y$ (eV, U=0 V)	$NiFe(OH)_xCl_y$ (eV, U=1.23 V)	$NiFeO_xH_y$ (eV, U=0 V)	$NiFeO_xH_y$ (eV, U=1.23 V)
**	0	0	0	0
OH	0.47995	-0.75005	1.68489	0.45489
O	2.34257	-0.11743	3.39433	0.93433
*O*OH	3.77497	0.08497	5.2892	1.5992
OO	4.60336	-0.31664	6.77907	1.85907
$**+O_2$	4.92	0	4.92	0

Table S10. Comparison of AEMWE performance among reported Ni/Fe-based anodes in alkaline media.

AEMWE	Voltage	Stability	Temperature	Ref.
$NiFe(OH)_xCl_y$|| Pt/C	**1.69 V@1 A cm^{-2} (without iR compensation)**	**1000 h@1 A cm^{-2}**	60 ℃	**This work**
PW_{12}-CoFe LDH||Pt/C	2.3 V@1 A cm^{-2}	1000 h@1 A cm^{-2}	60 ℃	***Nat. Commun.*** 2025, 16, 5541
NiFe-SQ/NF-R|| Pt/C	1.9 V@1 A cm^{-2}	100 h@1 A cm^{-2}	25 ℃	***Nat. Commun.*** 2025, 16, 3407
$V_{Cr,Co}$-NiFeOOH||Pt-NiCoP	1.76 V@1 A cm^{-2}	500 h@0.5 A cm^{-2}	25 ℃	***J. Am. Chem. Soc.*** 2025, 147, 3, 2607–2615
CFMO-2||Pt/C	1.65 V@1 A cm^{-2}	100 h@1 A cm^{-2}	80℃	***Angew. Chem. Int. Ed.*** 2025, 64, e202416141
NiFe(S)/NM|| $MoNi_4$	1.74 V@1 A cm^{-2}	23 h@0.3 A cm^{-2}	60 ℃	***Angew. Chem. Int. Ed.*** 2025, 64, e202500303
NiFe-LDH/Ni_4Mo|| NiFe-LDH/Ni_4Mo	1.76 V@0.3 A cm^{-2}	150 h@0.1 A cm^{-2}	25 ℃	***Angew. Chem. Int. Ed.*** 2025, 64, e202413250
Ru-S-NiFe LDH||Pt/C	1.92 V@1 A cm^{-2}	80 h@1 A cm^{-2}	55 ℃	***Adv. Energy Mater.*** 2025, 2500554
NiFeS||Pt/C	1.78 V@1 A cm^{-2}	300 h@1 A cm^{-2}	60 ℃	***Adv. Funct. Mater.*** 2025, 2506656
NFMN-FeOOH|| NFMN-Ni_2P	1.81 V@0.5 A cm^{-2}	150 h@0.5 A cm^{-2}	25 ℃	***Adv. Funct. Mater.*** 2023, 2311854
NiFe-LDH-PTA	1.93 V@1 A cm^{-2}	170 h@1 A cm^{-2}	60 ℃	***ACS Catal.*** 2025, 15, 8, 6486–6496

Reference

[1] K. Heusler, S. Trasatti, J. Justice, **Pure and Appl. Chem.** 1986, 58, 955-966.